A Review of UAV-based Ground Penetrating Radar Systems

Yuri Álvarez López, María García-Fernández, Guillermo Álvarez-Narciandi, and Fernando Las-Heras Andrés, *Senior Member, IEEE*

***Abstract*—Advances in Unmanned Aerial Vehicles (UAVs) technology have fostered their use in a wide range of areas, such as agriculture and forestry, surveillance and security, and infrastructure inspection. One of the advantages of UAVs is their capability of conducting remote inspection and sensing by placing different kinds of sensors on board them. In this sense, UAV-based Ground Penetrating Radar (GPR) systems are of particular interest, as they bring together the advantages of UAVs and GPR, resulting in contactless subsurface sensing and imaging systems capable of performing a fast scanning of difficult-to-access scenarios.**

This contribution reviews the advances on UAV-based GPR systems, describing their architecture and subsystems. In particular, an analysis of different UAV-based GPR systems is presented, focusing on the technical solutions adopted in each case and the detection capabilities that have been achieved. Attention will be also given to the methodologies implemented to obtain 3D high-resolution images of the underground. Finally, the main challenges faced by these systems concerning further improvements of the scanning throughput and the detection accuracy will be discussed.

***Index Terms*—Unmanned Aerial Vehicles, Ground Penetrating Radar, Synthetic Aperture Radar, archaeology, landmine detection, Improvised Explosive Devices detection, snow depth, search and rescue missions.**

I. Introduction

UNMANNED Aerial Vehicles (UAVs) have been steadily introduced in a vast variety of sectors, e.g. surveillance and security [1], agriculture and forestry [2], [3], geosciences [4], [5], or infrastructure inspection [6], [7]. Their success is mainly based on their capability to reach difficult-to-access areas, as well as their relative ease of use and operation (especially compared to manned aircraft systems). Furthermore, improvements in terms of battery life and payload capacity have enabled the capability of integrating complex sensors on board UAVs [5].

Although up to date a large amount of UAV-based applications still rely on images and videos taken with optical cameras, other UAV-based applications based on more specific sensors are being developed. Sensors to measure temperature [8], electromagnetic field intensity [9], [10], the presence of a particular gas in the air [11], or ultrasound sensors for contact inspection [7] have been integrated within UAV platforms, yielding novel remote sensing applications. Among these sensors, hyperspectral cameras have been of particular interest in the fields of agriculture and forestry, and infrastructure inspection [12]. The state-of-the-art of UAV-based systems for high-frequency measurements is reviewed in [10], covering topics such as airborne antenna measurements, direction finding and interference hunting, and mobile network testing. Advances in UAV systems in which the payload consists of a radar sensor is presented in [13], focusing on radar hardware and processing techniques. Several application examples are also presented in [13] to illustrate the operation and performance of these UAV-based radar systems.

Concerning UAV-based radar systems, some prototypes have been successfully introduced for Synthetic Aperture Radar (SAR) imaging, as described in [14]–[16]. It is also worth mentioning the prototype presented in [17] based on a relatively small consumer drone, and the system described in [18], which achieves 2 cm cross-range resolution by means of a 77 GHz radar together with motion compensation techniques. UAV-based Interferometric SAR (InSAR) systems, devoted to obtaining accurate digital elevation models, have been described in [19] and [20].

Depending on the soil composition and the working frequency band used by the radar module on board the UAV, underground detection and imaging capabilities can be achieved. The most evident application of UAV-based systems providing subsurface detection and imaging is the safe detection of buried threats such as landmines and Improvised Explosive Devices (IEDs) [21]. The use of UAVs avoids contact between the sensors and the scanned area, minimizing the risk of accidental detonation. Actually, the detection of buried explosive threats is perhaps the application area that has impulsed the most the development of UAV-based systems for underground detection, as described in [21].

There are different sensors that can be used to detect buried targets, but Ground Penetrating Radar (GPR) is doubtlessly the most widely used technology for subsurface sensing and imaging [22]. GPR has been introduced in a wide scope of applications, such as infrastructure monitoring [23], archaeology [24], and security and defense [25]. Part of the GPR success lies in the capability to overcome the limitations of metal detectors [26], [27] and magnetometers [28], which are unable to detect non-metallic targets. In fact, among the sensors and

The authors are with the Area of Signal Theory and Communications, Department of Electrical Engineering, University of Oviedo, Gijón, 33203, Spain. e-mail: alvarezyuri@uniovi.es.

This work has been partially funded by the Ministry of Defense - Government of Spain and by the University of Oviedo under Contract 2019/SP03390102/00000204 / CN-19-002 ("SAFEDRONE"); by the Ministerio de Ciencia, Innovación y Universidades of Spain under Project RTI2018-095825-B-I00; by Gobierno del Principado de Asturias under Project IDI/2021/000097; by European Union NextGenerationEU fund under project MU-21-UP2021-030; and by the Universidad de Oviedo under grant GR-2010-0015.

Manuscript received XXXXX, 2021; revised XXXXXXX, 2022.

systems compared in [21] for IED and landmine detection (radar-based methods like GPR and SAR, magnetometer-based systems, metal detectors, thermal imaging, ultrasound detectors, and other sensors that exploit the vapor signature of explosives within landmines and IEDs), GPR provides one of the best detection performances (see Table V of [21]).

In brief, the operation principle of GPR is the reflection of electromagnetic waves due to changes in the constitutive parameters (conductivity, σ, and permittivity, ε) of materials [22], [29], [30]. Depending on whether the GPR transmitting and receiving antennas are in contact with the ground or not, GPR systems can be classified into ground-coupled GPR (Fig. 1 (a)) and air-launched GPR systems [31], [32] (Fig. 1 (b,c)). The latter have been integrated within UAV platforms resulting in UAV-based GPR systems (Fig. 1 (c)).

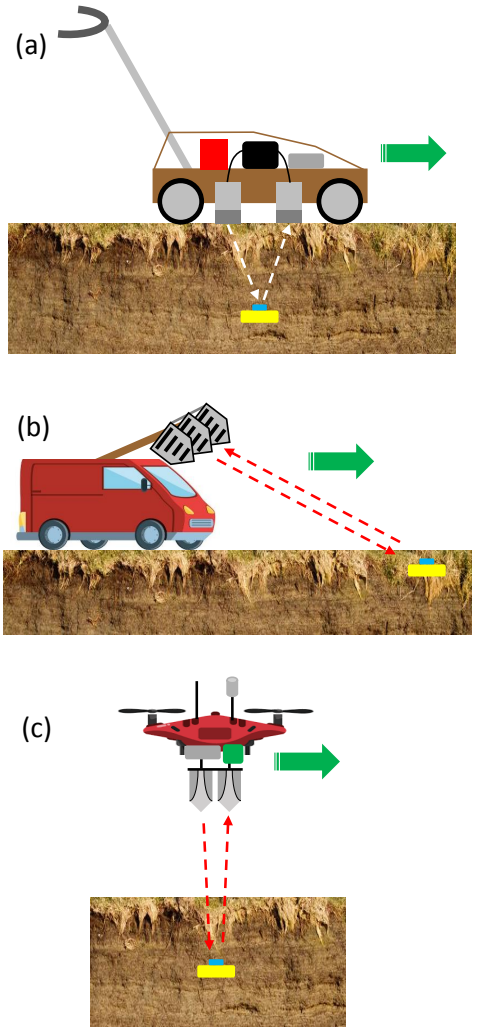

Fig. 1. Examples of different GPR architectures: (a) ground-coupled GPR, (b) air-launched GPR mounted on a ground vehicle, (c) air-launched GPR on board a UAV.

Despite improvements in UAV and GPR technologies in terms of miniaturization, functionalities, reliability, and affordability, the integration of a GPR on board a UAV is not straightforward and requires addressing several challenges, some of them inherent to air-launched GPR systems:

- The dynamic range of air-launched GPR systems is limited by the impedance mismatch between the air and the ground, and by the propagation losses between the transmitting (Tx) and receiving (Rx) antennas and the soil [32], [33].
- There is a deviation between the predefined flight path and the actual flight path followed by the UAV (which contains the points where GPR measurements are taken). These deviations are mainly due to wind gusts and the flight control system of UAVs acting on the throttle of the propellers to adjust or correct the UAV position and attitude. Thus, GPR processing techniques capable to handle non-canonical acquisition grids are required.
- GPR measurements must be geo-referred with sufficient accuracy for the proper detection of buried targets. In addition, GPR systems implementing SAR-based processing techniques require particularly a high geo-referring accuracy. Depending on the value of the highest frequency within their working frequency band, the required accuracy can be smaller than a few centimeters.
- The limitations on size and weight of the payload impose restrictions on the kind of devices that can be integrated on board the UAV. These limitations also determine the flight time, and thus the size of the area that can be scanned in a single flight.

This contribution presents a review of UAV-based GPR systems for subsurface sensing and imaging, complementing the reviews published in [13] about airborne-based radar systems, and in [10] about high-frequency measurements with UAVs. Details about the technical features of these systems will be presented and discussed according to the authors' experience in the development of UAV-based GPR prototypes. The technical issues analyzed in this review are also complementary with previous review articles like [32], which was focused on GPR processing techniques for airborne-based GPR systems. Additionally, some of the issues raised in [32] about UAV challenges for air-launched GPR systems, like the extension of two-dimensional (2D) approaches to full three-dimensional imaging (3D), are addressed in this review.

This article is structured as follows: Section II describes the basic components of UAV-based GPR systems, presents their main architectures, and gives an overview of UAV-based GPR processing flowcharts, focusing on 3D imaging capabilities. This section also presents the acquisition schemes that can be implemented, discussing their advantages and limitations. A review of different UAV-based GPR prototypes is conducted in Section III, describing their technical specifications and linking them with their detection capabilities within their targeted application. Section IV presents an application example of a UAV-based GPR system for landmine detection. Finally, challenges and future trends are discussed in Section V.

II. An overview of UAV-based GPR systems

A. Elements of a UAV-based GPR system

Conceptually, a UAV-based GPR system can be understood as a UAV whose payload is a GPR module. Indeed, as it will be explained in Section II-A, subsection 4 "Design and

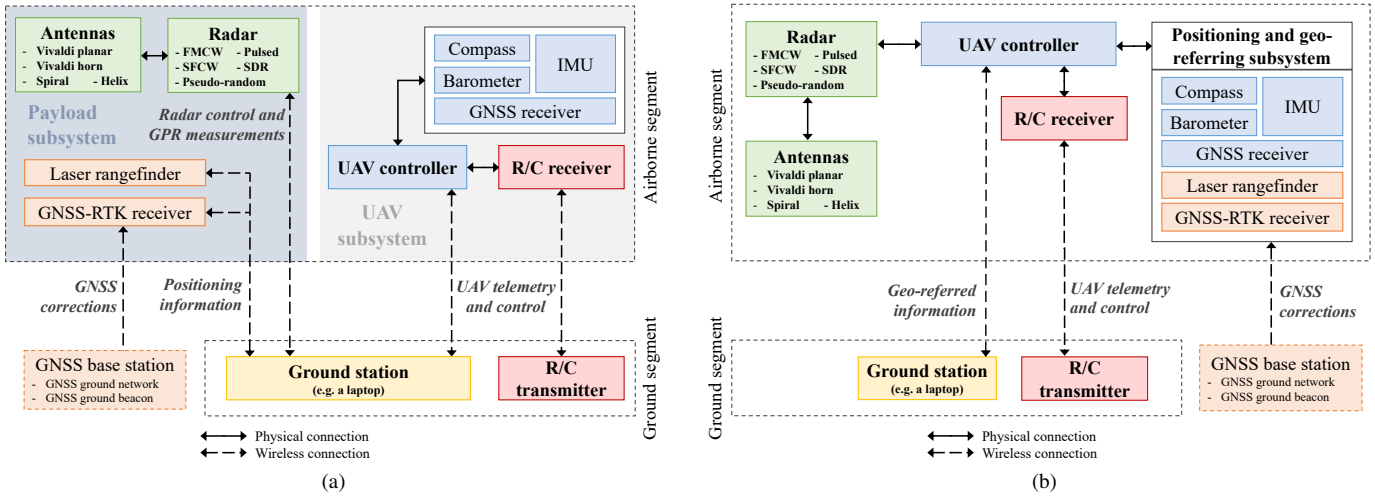

Fig. 2. Scheme illustrating the architecture of (a) a UAV-based GPR system with the GPR payload independent of the UAV, and (b) of a UAV-based GPR system with the GPR payload integrated within the UAV. The main components of each subsystem are depicted in a specific color: GPR subsystem in green, flight control and basic positioning sensors in blue, high-accuracy positioning sensors in orange, communications subsystem in red, and ground station in yellow. Connections between the different subsystems and devices are also indicated.

implementation approaches", this is one of the implementation strategies that can be adopted (where the payload is independent from the UAV, Fig. 2a), whereas the other approach consists of a complete integration of the GPR subsystem within the UAV (Fig. 2b). Regardless of the architecture, the following elements and subsystems can be identified in any UAV-based GPR system:

- A flight control subsystem, composed of a UAV flight controller and, in some cases, a micro-computer (e.g. a Raspberry Pi).
- A positioning and geo-referring subsystem, composed of, at least, an Inertial Measurement Unit (IMU), a barometer, a compass, and a Global Navigation Satellite System (GNSS) receiver.
- A communications subsystem between the UAV and the pilot and, in some cases, between the UAV and a ground station (typically a device with computing capabilities, e.g. a laptop or a tablet). At least, it includes the radio controller (R/C) transmitter and receiver modules.
- The GPR subsystem, whose main components are the radar module and the transmitting and receiving antennas.

1) Positioning and geo-referring subsystem: Accurate positioning and data geo-referring is of utmost importance for certain UAV-based applications. This is the case of GPR measurements, as the positioning and geo-referring accuracy limits the resolution of the system, and thus the minimum size of the targets that can be detected. If geo-referring uncertainty is significantly smaller than the smallest GPR wavelength, then, SAR processing techniques can be applied. This results in a better focusing than the one that would be achieved by the GPR antennas by themselves [34], which is related to the fact that cross-range resolution is better when SAR processing is used. The relationship between geo-referring accuracy and the GPR-SAR resolution is discussed in Section II-D.

The minimum set of positioning sensors on board the UAV (IMU, barometer, compass, and basic GNSS receiver) can provide positioning accuracy ranging from tens of cm up to several meters. Thus, if cm-level accuracy is required, additional positioning sensors are needed.

The majority of UAV-based GPR systems are conceived to operate outdoors. Thus, cm-level accuracy GNSS systems can be used for these applications. In this regard, GNSS Real Time Kinematics (GNSS-RTK) has been rapidly adopted in the field of UAVs [35] thanks to its capability of providing real-time positioning with cm-level accuracy. The popularization of GNSS-RTK has contributed to lowering the prices of GNSS-RTK receivers at a rate similar to the improvements introduced in new GNSS-RTK modules (e.g. support for GNSS dual and triple frequency bands) [36].

A GNSS-RTK requires, at least, a receiver module mounted on board the UAV and another receiver, placed on the ground at a fixed position, to act as a base station. The ground receiver can be another GNSS-RTK module similar to the one on board the UAV, or it can be a node of a GNSS regionwide or nationwide ground network of GNSS stations. Apart from GNSS-RTK, another GNSS-based method that can be used for accurate positioning is Precise Point Positioning (PPP). Its main drawback is the long convergence time, limiting its use for real-time positioning [37].

Concerning the vertical or height accuracy, GNSS information is based on a reference geoid (e.g. the World Geodetic System 1984, WGS84) that does not represent local variations of the terrain profile. That is, GNSS height corresponds to the height over the geoid, not over the terrain. Thus, when large areas are scanned, GNSS height information is not accurate enough for GPR processing. Therefore, additional sensors, such as laser rangefinders, have to be placed on board the UAV to retrieve the ground profile. To illustrate this, a comparison between the ground profile obtained using GNSS-RTK information, a laser rangefinder sensor, and a

radar altimeter is shown in Fig. 4 of [38].

2) GPR subsystem: The GPR subsystem is composed of a radar module connected to a set of antennas that sends the radiofrequency signals generated by the radar module towards the ground, and collects the electromagnetic waves reflected on the ground and in the objects buried in it. Raw GPR measurements can be sent to the ground station in real-time or stored on board the UAV (to be downloaded after the flight). Processing of GPR measurements is usually conducted in the ground station or in a workstation due to the computational burden associated with the GPR processing techniques.

In GPR systems, there is a trade-off between range resolution and penetration depth. Range or depth resolution is proportional to the frequency bandwidth of the GPR system. In this regard, the use of higher frequencies enables broader bandwidths. Conversely, the penetration depth of the electromagnetic waves in the soil depends on the working frequency of the GPR as well as the soil constitutive parameters. To illustrate this, Figure 1 of [39] provides an estimation of the expected penetration depth as a function of the frequency and soil moisture content. For example, at a frequency of 3 GHz, the penetration depth ranges from 0.5 m (dry soils, soil moisture 1 %) to a few cm for wet soils (soil moisture 30 %). In addition to this, the choice of the working frequency band is related to the radar module and the kind of antennas to be mounted on board the UAV.

In general, UAV-based GPR systems can be classified into two main groups based on the kind of radar technology. Several implementations of UAV-based GPR systems have opted for continuous wave radars, either Frequency Modulated Continuous Wave (FMCW) or Stepped Frequency Continuous Wave (SFCW) [40]. Their main advantage is their simplicity in terms of hardware implementation. Other UAV-based GPR prototypes make use of time-domain radar modules, either impulse-like or transmitting pseudo-random signals. These radars send mostly Ultra Wide Band (UWB) signals and they might provide a better signal-to-noise ratio than continuous wave radars [41], [42].

Antennas are one of the major challenges when designing and implementing UAV-based GPR systems. Antenna size and weight are closely related to its working frequency band: the lower the frequency, the larger (and heavier) the antenna is. Thus, planar or horn-like antennas are good candidates for these airborne systems thanks to their balance between size, weight, and radiation performance. Unlike ground-based GPR systems, cavity-backed spiral antennas are not suitable for UAV-based GPR prototypes as they are designed to match the air-ground interface impedance, so their performance in air-launched GPR systems is worsened.

3) Communications subsystem: The communications subsystem comprises at least the radio control, consisting of a transmitter module within the UAV remote controller, and a receiver module on board the UAV. Typical frequencies of operation for the radio controller (R/C) are $433\,\text{MHz}$, $868\,\text{MHz}$, and $2400 - 2500\,\text{MHz}$. UAV R/C systems usually take advantage of frequency hopping spread spectrum (FHSS) techniques to reduce interferences with other in-band radio transmissions. Apart from the commands to control the flight of the UAV, it is typical to transmit telemetry data using this radio link. Alternatively, a dedicated data link between the ground station and the UAV to transmit telemetry data and the GPR measurements can be deployed. For example, a Wireless Local Area Network (WLAN) operating in the $2.4\,\text{GHz}$ and/or $5.8\,\text{GHz}$ frequency bands can be used.

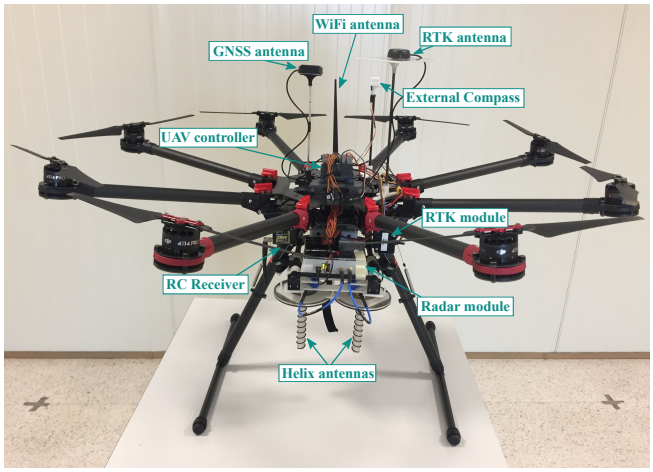

Fig. 3. An example of a UAV-based GPR system depicting the main subsystems and components [44].

4) Design and implementation approaches: Payload integration on board the UAV can be conducted under two different approaches. On the one hand, the payload can be designed to be fully independent from the UAV platform. This design methodology is illustrated in Fig. 2a, where the airborne segment is divided into two independent parts: the payload subsystem and the UAV subsystem. Under this approach, the payload can (must in some cases) include its own positioning subsystem for GPR measurements geo-referring. On the other hand, the UAV and the payload can be designed and implemented altogether, resulting in the architecture shown in Fig. 2b. This architecture requires direct access to the UAV controller.

The main advantage of an independent payload with respect to a payload integrated within the UAV is the possibility of placing it in different UAV platforms and models, requiring little modification of the software. However, it still requires designing and manufacturing an appropriate interface to adapt the payload to the UAV frame. On the other side, a payload integrated within the UAV makes easier the synchronization between the different subsystems and enables the UAV to use the high-accuracy geo-referring system also for navigation, without the need of duplicating these sensors. UAV systems that incorporate state-of-the-art sensors or require ad hoc flight operation modes are usually implemented following this approach [43].

A picture of a prototype of a UAV-based GPR system is shown in Fig. 3, where the main elements and subsystems are indicated. In this prototype, two helix antennas with reverse handedness have been used for the GPR subsystem [44].

B. Architectures of UAV-based GPR systems

Air-launched GPR systems can be classified into three main groups according to the orientation of the GPR antennas with respect to the ground (as illustrated in Fig. 4). As UAV-based GPR systems are a subgroup of air-launched GPR systems, the same classification applies to them.

- Forward-looking GPR (FLGPR): the GPR antennas are pointing towards the ground with oblique/near-grazing incidence. This helps to reduce reflections from the air-ground interface [32], [45], [46]. The main advantages of FLGPR systems are: i) clutter due to the reflection on the ground is minimized, as it is scattered away from the incident angle; ii) in the case of a FLGPR mounted on a ground vehicle (Fig. 1 (b)), a safe distance between the scanned area and the vehicle can be kept, which is significantly important in the field of explosive threats detection.
- Side-looking GPR: it is similar to FLGPR, with the GPR antennas also tilted with respect to the air-soil interface to minimize specular reflection. However, unlike FLGPR, the vehicle where the GPR is assembled does not move in the same direction towards the antennas are pointing at. Instead, it moves laterally [47] or describing a circular path (Circular SAR, CSAR) [48]–[50], as illustrated in Fig. 4.
- Down-looking GPR (DLGPR): in this architecture, GPR antennas are pointing perpendicular to the soil surface [32], [33], [51] (Fig. 1 (c)). As the antennas are usually closer to the inspected area, this results in smaller free-space propagation losses than in FLGPR systems, but at the expense of a stronger reflection of electromagnetic waves at the air-soil interface. Depending on the range or depth resolution of the DLGPR system, the reflection at the air-soil interface might mask shallow targets. An additional advantage of DLGPR systems is related to electromagnetic interferences, a concern stressed in [52]. As the GPR antennas are pointing downwards, in-band interferences to and from other radiofrequency sources within the vicinity of the UAV are minimized with respect to FLGPR and side-looking GPR architectures.

The choice of the GPR architecture to be placed on board the UAV depends on the kind of scenario to be surveyed. For example, in the case of shallow targets, a FLGPR or side-looking GPR could provide better detection capabilities than DLGPR architectures as the air-soil clutter is minimized. However, for deeper targets, DLGPR is likely to provide better results than FLGPR because of the greater dynamic range. A comparison of the imaging capabilities of DLGPR and FLGPR systems is presented in [53] and [54]. These contributions also introduce a hybrid GPR architecture that combines the advantages of FLGPR (minimization of air-ground reflection) and DLGPR (greater dynamic range).

C. GPR processing techniques for UAV-based systems

Processing techniques for GPR measurements taken with a GPR on board a UAV are based on those developed for air-launched GPR systems, the latter being described in [32].

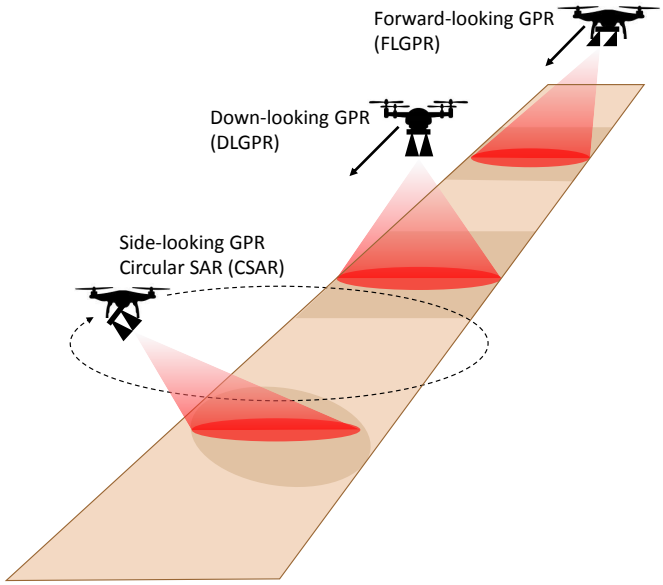

Fig. 4. Illustration of UAV-based GPR scanning architectures.

Additional processing steps are required to address the specific issues affecting UAV-based measurement systems.

Regardless of the architecture of the UAV-based GPR system, the GPR processing flowchart can be summarized as shown in Fig. 5. The first step comprises the processing of the positioning information and the pre-processing of the acquired radar measurements. This may include the selection of a subset of measurements which were acquired over the region of interest, the discard of samples that do not meet a certain condition (e.g., if when they were acquired the UAV was too high), the application of techniques to refine the available positioning data, and the use of filtering and clutter removal techniques (time-gating, average subtraction [55], [56] or Singular Value Decomposition (SVD)-filtering [51], [57], among others).

Once the pre-processing of the radar measurements is completed, GPR processing algorithms to recover 2D or 3D images of the underground and potential targets buried in it are applied. Some of these algorithms will be explained in Section II-D. The recovered 2D or 3D images can be further processed using automatic target recognition (ATR) techniques. ATR has been a key research topic within the GPR framework, including techniques that range from Constant False Alarm Rate (CFAR) detectors [49], [58] to Convolutional Neural Networks (CNN) [59].

As previously mentioned, deviations between the predefined flight path and the actual one are likely to occur due to perturbations like wind gusts, or corrections of the trajectory conducted by the UAV controller. The result is that measurements are distributed on an irregular, non-uniformly sampled domain. This issue is especially critical when a coherent combination of the GPR measurements is conducted (the insight of this will be discussed in Section II-D) and, as a consequence, measurement data processing methods for UAV-based systems have to address the issue of non-regular

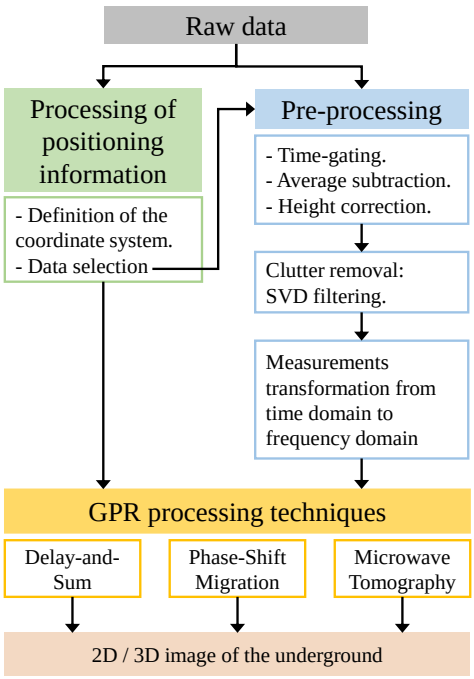

Fig. 5. Processing flowchart for UAV-based GPR measurements.

sampling of the scanned area.

The generic GPR processing described in this Section can be tailored to each UAV-based GPR system architecture and the targeted application, including also complementary techniques to improve the detection capabilities. For example, [51] includes additional steps like the equalization of the frequency response of the radiofrequency components of the GPR subsystem, and the application of a processing gain technique to enhance the response (i.e. the reflectivity) of deeply buried targets. In [20], radar measurements collected with the implemented prototype are used to obtain a digital elevation model of the scanned area to improve GPR processing. In this UAV-based GPR system, two different frequency bands are considered: the lower band ($1-4\,$GHz) is used for subsurface scanning and the upper band ($6-9\,$GHz) to map the soil profile.

D. GPR-SAR imaging

One of the main challenges faced by UAV-based GPR systems is the retrieval of high-resolution images of the subsoil and the objects buried in it. For a single measurement position, the depth or range resolution, Δr, is given by the frequency bandwidth. Under free-space considerations, Δr is

$$\Delta r = \frac{c}{2(f_{max} - f_{min})}, \tag{1}$$

being f_{min} and f_{max} the lower and upper limits of the frequency band (c is the speed of light in free space).

For a two-dimensional or three-dimensional scanning, lateral or cross-range resolution depends on how focused the transmitted and received electromagnetic waves are. If we consider an aperture antenna pointing perpendicular to the scanned area, the free-space cross-range Δl resolution is given by

$$\Delta l = \frac{R\lambda_c}{L_{ap}}, \tag{2}$$

where R is the distance between the measurement domain and the target, $\lambda_c = 2c/(f_{min} + f_{max})$ is the wavelength at the central frequency, and L_{ap} denotes the width of the aperture.

Thus, the wider the GPR bandwidth and the antenna aperture, the better the resolution of the GPR system is. As mentioned in Section II-A, subsection 2 "GPR subsystem", the choice of the GPR working frequencies must reach a balance between the desired range resolution, the size and weight of the GPR subsystem hardware (UWB antennas mainly), and the targeted penetration depth. In Section III it will be shown that current UAV-based GPR systems can achieve bandwidths up to $5.5\,$GHz, yielding $\Delta r = 2.7\,$cm in free-space.

Cross-range resolution can be improved by means of electrically large aperture antennas or antenna arrays. However, as stated before, restrictions in size and weight of the UAV payload limit the possibility of placing such large antennas on board the UAV. Thus, other strategies to increase cross-range resolution, without jeopardizing the performance and operation of UAV-based GPR systems, are required.

Taking advantage of the fact that the GPR is mounted on a moving platform (a UAV in this case), SAR processing can be conducted. The underlying idea is to create a virtual antenna array by coherently combining measurements collected at the different positions of the path followed by the UAV. Thus, the cross-range resolution achieved with SAR processing can be calculated with (2) by replacing L_{ap} with the size of the synthetic aperture.

An example of a GPR processing technique is the Delay-and-Sum (DAS) or backprojection method, which consists of adding all measurements coherently at one focal point, repeating this procedure in all the points of the targeted scenario [60]. Under the assumption of a monostatic or quasi-monostatic configuration, the reflectivity of a point located underground, $\rho(r')$, can be calculated from the scattered field measured at N acquisition points within a frequency band discretized into M frequencies, $E_{scatt}(r_n, f_m)$, as

$$\rho(r') = \sum_{n=1}^{N}\sum_{m=1}^{M} E_{scatt}(r_n, f_m) e^{+j2(\phi_0+\phi_1)}, \tag{3}$$

where r_n is the position where the *n*-th measurement was acquired, f_m is the *m*-th discrete frequency, and ϕ_0, ϕ_1 are the phaseshifts due to the wave propagation in the air and in the soil. These phaseshifts are defined as

$$\phi_0 = k_{0,m}||r_{i,n} - r_n||_2, \tag{4}$$

and

$$\phi_1 = k_{0,m}\sqrt{\varepsilon_r}\;||r' - r_{i,n}||_2, \tag{5}$$

respectively, where $k_{0,m}$ is the free-space wavenumber for the m-th discrete frequency, ε_r is the relative permittivity of the soil, and $r_{i,n}$ is the refraction point on the air-ground interface.

The position of the refraction point $r_{i,n}$ can be derived from Snell's law solving a fourth-order equation. To reduce the complexity and computational time, several approximations have been proposed [60]. The calculation of the refraction point in the case of multi-layered soils is described in Section II.A of [55].

If free-space propagation is considered, then (4) and (5) can be simplified as follows:

$$\phi_0 + \phi_1 = k_{0,m}||r' - r_n||_2. \tag{6}$$

One of the advantages of DAS is the capability of handling arbitrary-shape, arbitrary-sampled acquisition domains. The only restriction is that acquisition points must fulfill the Nyquist sampling rate, that is, the separation between adjacent positions must not be greater than $\lambda_{min}/2$, with $\lambda_{min} = c/f_{max}$. Thus, DAS is suitable for UAV-based GPR measurements because, as stated in Section II-C, GPR measurements are likely to present an irregular sampling pattern due to small deviations of the UAV from the pre-defined flight path [51].

Phase Shift Migration (PSM) or $\omega - k$ migration is another formulation that has been successfully tested with UAV-based GPR measurements. This formulation is derived from the electromagnetic wave equation and can also take into account the constitutive parameters of the ground [61], [62]. It is computationally more efficient (and hence faster) than DAS, as the backpropagation operation is performed in the k-spectral domain, enabling the use of Fast Fourier Transform (FFT) operations. Conversely, it requires evenly sampled acquisition domains. Thus, in the case of UAV-based systems, GPR measurements must be interpolated to a regular grid before the application of PSM. An example of PSM applied to GPR measurements taken with a UAV-based GPR system is presented in [63], achieving up to 23 times speed-up with respect to DAS. Another example of PSM or $\omega - k$ migration processing for UAV-based GPR measurements can be found in [64].

In terms of accuracy, the interpolation of GPR measurements to a regular grid does not have an impact on the recovered GPR-SAR images, provided the scanned area is properly sampled (that is, the spacing between consecutive points is equal or less than $\lambda/2$). A comparison of DAS and PSM has been conducted in [55] (Fig. 8 and Fig. 10) and in [63] (Fig. 5 to Fig. 8), finding that there are no significant differences between both methods from a qualitative point-of-view.

Apart from PSM and DAS, other GPR data processing techniques that could be suitable for UAV-based GPR systems are:

- Piecewise Synthetic Aperture Radar (P-SAR): it is a modified version of the PSM algorithm that uses the reflection and transmission coefficients of electromagnetic waves when passing through the different layers of the ground [65].
- Wiener filter-based GPR-SAR: in this technique, the Green's functions for layered media are introduced in the formulation. [65].
- Integral equation-based formulations: they relate the measured scattered field and the constitutive parameters (conductivity, permittivity) of the investigation domain through the electromagnetic integral equations. Integral equation-based techniques require solving a full-wave inverse problem, which can be ill-posed and computationally expensive to solve.
- Microwave tomography approaches: they are based on the solution of a linear version of the integral equations relating the scattered fields and the investigation domain. The development of solving strategies for this inverse problem has been widely addressed in the literature [32], [66], being recently introduced in the area of UAV-based GPR systems [67].

Regardless of the considered GPR processing technique, the coherent combination of the measurements requires the acquisition points to be accurately geo-referred to minimize uncertainties that would distort the recovered SAR image. Position uncertainties will have an impact on the recovered GPR-SAR images, being their degradation proportional to the size of the synthetic aperture. This effect is shown in Fig. 11 of [44] (Fig. 11 (b), aperture length of 70 cm, and Fig. 11 (c), aperture length of 230 cm).

To illustrate the basics of GPR-SAR processing and, in particular, to stress how its usage in UAV-based GPR systems significantly improves their cross-range resolution (and thus their detection capabilities), results obtained from GPR measurements performed in a controlled environment are presented next. A picture of the measurement setup is shown in Fig. 6. The scenario under test is a plastic box filled with sand (ε_r between 2.5 and 3) with two 8 cm diameter metallic disks buried approximately $9-10$ cm deep. The measurement system is composed of a Vector Network Analyzer (VNA) connected to a pair of helix antennas with reverse handedness. The working frequency band ranges from 3 GHz to 6 GHz [68]. Measurements were conducted on a 90 cm $\times$ 100 cm planar acquisition grid, sampled every 2.5 cm (i.e. $\lambda/2$ at the upper frequency, 6 GHz). This plane will be taken as the zero reference for the z axis (i.e., $z = 0$ m). Measurements were processed with the DAS technique considering free-space propagation (i.e. $\varepsilon_r = 1$).

The reflectivity retrieved from the measurements when GPR-SAR processing is not applied is depicted in Fig. 7. This reflectivity corresponds to the raw measurement located at the same (x, y) coordinates. Thus, cross-range resolution is given by the beamwidth of the transmitting and receiving antennas, which is wider than the beamwidth of the synthetic aperture. As observed in Fig. 7, cross-range resolution given by the antenna beamwidth is not sufficient to distinguish the buried metallic disks, and only the profile of the sand box can be inferred (Fig. 7 (a)).

Results corresponding to GPR-SAR processing, i.e., when measurements on the acquisition domain are coherently combined, are depicted in Fig. 8. According to (2), the cross-range resolution for this setup is $\delta l \sim 5$ cm. Therefore, both metallic

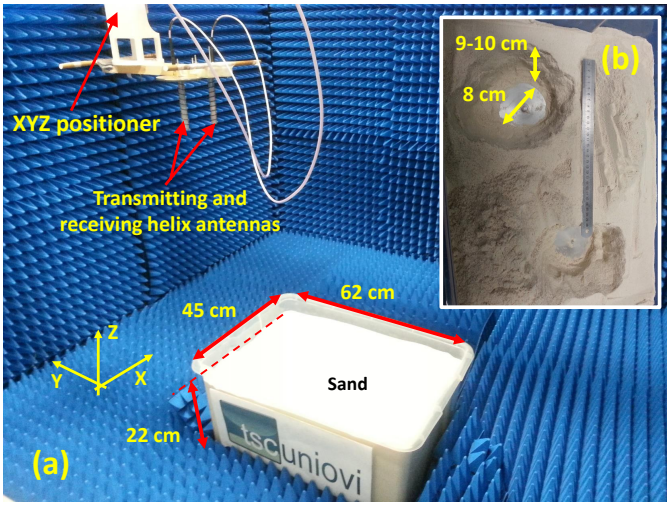

Fig. 6. Picture of the GPR measurement setup (a) and the two 8 cm diameter metallic disks buried in a sand box (b).

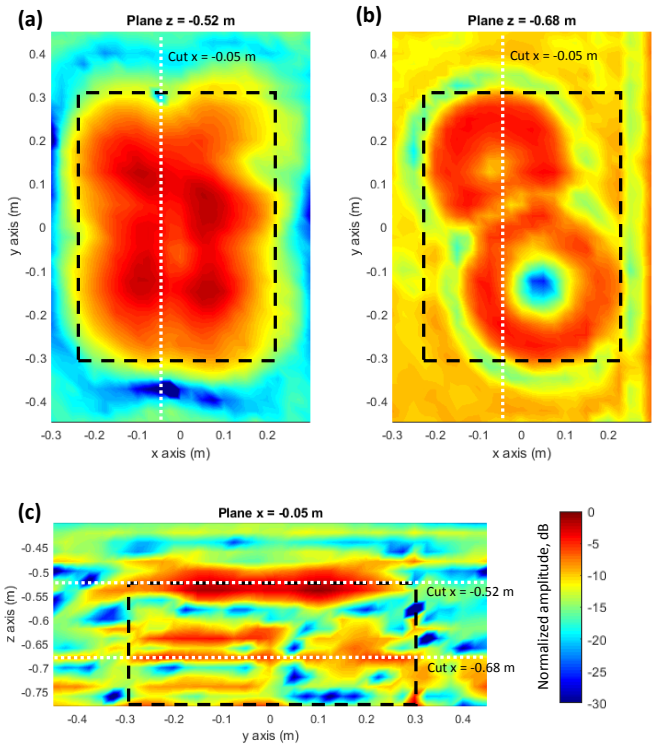

Fig. 7. GPR imaging results when no GPR-SAR processing is applied to the measurements. Horizontal cuts of the reflectivity at $z = -52\,\text{cm}$ (a) and $z = -68\,\text{cm}$ (b). Vertical cut, YZ plane, at $x = -5\,\text{cm}$ (c).

disks are well-focused in the resulting image and are clearly distinguishable from each other (Fig. 8 (b) and (c)).

In this scenario, the targets are buried deeper than the range or depth resolution ($\delta r = 5\,\text{cm}$ in free-space, 1, or $2.9-3.2\,\text{cm}$ if the permittivity of the sand is taken into account [32], [68]). Thus, as observed in Fig. 8 (c), the reflection happening at the air-sand interface does not mask the response from the buried targets.

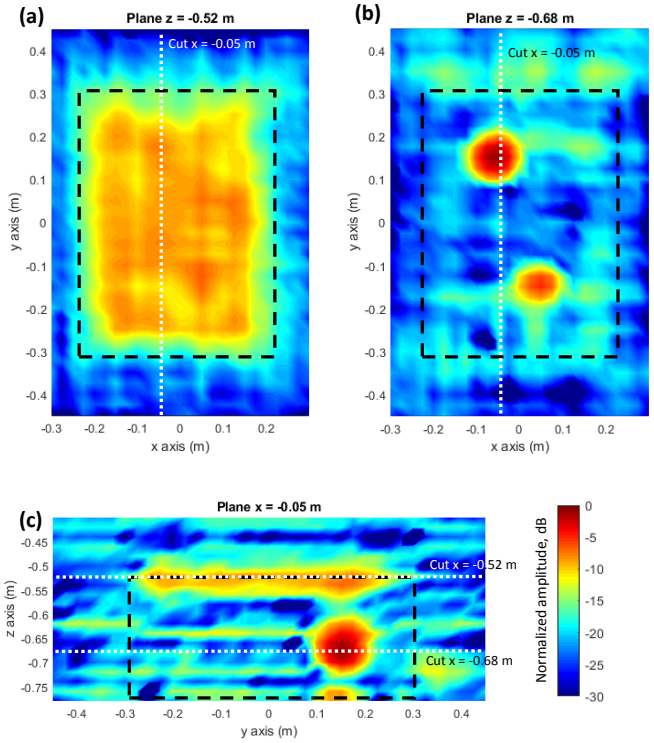

Fig. 8. GPR imaging results when GPR-SAR processing is applied to the measurements. Horizontal cuts of the reflectivity at $z = -52\,\text{cm}$ (a) and $z = -68\,\text{cm}$ (b). Vertical cut, YZ plane, at $x = -5\,\text{cm}$ (c).

III. A REVIEW OF UAV-BASED GPR ARCHITECTURES

Once the main features of UAV-based GPR systems have been described, the next step is the review of the different UAV-based GPR prototypes presented in the literature. A summary of the technical specifications extracted from the publications where these prototypes are described is presented in Table I. In particular, the information listed in the table is related to the working frequency band, the architecture and radar technology, and the use of SAR-like processing. A brief description of the validation scenario (characteristics of soil, size of the scenario, and/or information about the buried targets) and the flight operation mode are also included.

Analyzing the first column of Table I, it can be observed that the detection of IEDs and landmines is the primary area of application of UAV-based GPR systems, as outlined previously in Section I. Although in [32] it was stated that UAV-based GPR systems for IED and landmine detection were still at an early development stage, the fact is that several of the prototypes listed in Table I already provide 3D subsurface imaging capabilities [20], [49], [51], [69]. At least one of them has even been tested in realistic environments [58]. Geoscience and remote sensing is another area of application of some of the UAV-based GPR systems of Table I. In particular, they have been used for snowpack thickness measurement [70], [71], remote sensing of snow water equivalent [64], [72], characterization of different kinds of rocks [73], and soil moisture measurement [74]. Finally, avalanche victims search is another application where some of the developed prototypes have shown promising results [50].

Most of the UAV platforms chosen by the different research groups and companies working on UAV-based GPR systems consist of an hexacopter [20], [47], [49], [50], [67], [73], an octocopter [44], [51], [58], [70] or a coaxial quadcopter [69], [74], with a payload capacity up to 6-8 kg. This is the typical maximum payload weight of the majority of medium-size UAVs available in the civil market. The size and the maximum take-off weight of these UAV platforms provide an optimum trade-off between payload capacity and ease of operation, also avoiding the need for additional flight certifications required for heavier UAVs. UAV platforms [75] and [76] can be cited among the most popular ones for the development of customized UAV-based systems like the ones listed in Table I.

Concerning the GPR architecture, DLGPR has been adopted by the majority of the systems presented in Table I, being side-looking GPR the architecture adopted by almost all the remaining prototypes (bistatic common-offset architecture was also considered in [77], [78]). However, none of the analyzed systems implemented a FLGPR. A possible reason is that a FLGPR mounted on a ground-based vehicle still provides a safe standoff distance while overcoming some of the issues associated with UAV-based systems (e.g. limited flight time, payload size and weight restrictions, and operation subject to weather conditions). In the case of DLGPR, contactless operation cannot be easily achieved with ground vehicles, thus requiring airborne-based architectures. Another reason that could explain why DLGPR architecture is quite common among UAV-based GPR systems is related to the size of GPR antennas. Usually, bulky antennas are required to operate below $1000\,\text{MHz}$. In the case of FLGPR or side-looking GPR systems, antennas must be tilted with respect to the ground [47], [49], resulting in non-symmetrical, potentially unbalanced payloads. In DLGPR architectures, antennas are pointing downwards, making the design and assembly of a balanced, symmetric payload easier.

From the analysis of the working frequency bands of developed UAV-based GPR systems listed in Table I it can be concluded that the lower frequency limit (f_{min}) is around $500\,\text{MHz}$ - $1000\,\text{MHz}$. Typical GPR bandwidth ranges from $1000\,\text{MHz}$ - $1500\,\text{MHz}$ [69], [79] up to $3000\,\text{MHz}$ or wider [20], [47], [49]–[51], [70]–[72]. The use of these bandwidths results in a range or depth resolution equal or better than $5\,\text{cm}/\sqrt{\varepsilon_r}$. UAV-based GPR systems described in [73], [74], [81] make use of frequency bands with $f_{max} \leq 700\,\text{MHz}$ to achieve better penetration depth but at the expense of a narrower bandwidth than the rest of the systems analyzed in Table I.

In terms of radar technology, either CW (FMCW and SFCW) and time-domain radars (transmitting pulses or pseudorandom signals) have been considered as shown in Table I. These radar modules can be custom-built (e.g. [47], [79]) or general-purpose commercial radar modules ([44], [51], [70], [71], [73], [81]). The miniaturization of Vector Network Analyzers (VNA) has made their use on board UAVs feasible, as proved in [72], [74], although they are more expensive than CW radars. Software Defined Radio (SDR) technology provides a flexible, compact, and low-cost solution as described in [78], [83].

Concerning antenna choice, most of the UAV-based GPR systems of Table I make use of Vivaldi-like antennas (planar Vivaldi antennas [51], [58], [69], [77], [78] or Vivaldi horn antennas [49], [79]) as they exhibit good radiation properties (low dispersion, directive radiation pattern) within the working frequency band, while keeping size and weight suitable for assembly in a medium-size UAV.

Cross-range resolution is mainly determined by the capability of the UAV-based GPR system to provide measurements with enough positioning accuracy to enable SAR processing. Given the working frequency bands of the systems presented in Table I, positioning accuracy equal to or better than $2-3\,\text{cm}$ is required for coherent processing of the measurements. This is achieved by integrating cm-level accuracy positioning systems on board the UAV. For example, GNSS-RTK receivers are used in [20], [48], [50], also including a laser rangefinder in [44], [51], [58], [64], [70], [71].

Different flight schemes have been implemented in UAV-based GPR systems. The simplest one consists of a straight path over the surveyed area [44], [47], [70], [73], resulting in 2D range - cross-range images (i.e. these systems lack across-track imaging capabilities). The next step is to provide lateral or across-track cross-range resolution to enable 3D GPR imaging, which can be achieved in different ways depending on the system architecture. For example, DLGPR systems usually implement zig-zag flight paths [51], [58], [67], [74], [77], [78] (a video illustrating this flight scheme can be watched at https://bit.ly/3lZ974f). Those DLGPR systems implementing SAR processing techniques also require less spacing between consecutive along-track sweeps to prevent spatial aliasing in across-track direction [51], [58]. Most of side-looking GPR prototypes follow circular flight paths at different heights to create a cylindrical synthetic aperture surrounding the investigation domain [20], [49], [50]. In both cases, either zig-zag or circular flight paths, measurements collected within the surveyed area can be processed with a SAR method to recover 3D images of the underground.

Other implementation features of UAV-based GPR systems are related to the UAV controller and the operating system running in it. Customized UAV prototypes usually integrate UAV flight controllers running the open-source system Arducopter [44], [51], [58], [70], [71], thanks to the flexibility they provide for the integration of additional sensors like the GPR radar module, the GNSS-RTK receiver, and/or the laser rangefinder.

A. Review of detection capabilities

A review and discussion of the detection capabilities of some of the UAV-based GPR prototypes is presented in this subsection. Detection capabilities can be analyzed according to the soil composition, size and composition of the targets, and burial depth. Based on the description of the detection results of UAV-based GPR systems presented in the corresponding contributions, the following classification has been established: soils have been classified into sandy or dry soils (typical ε_r smaller than 4-5), and loamy soils (ε_r greater than 4-5). According to their size, targets have been grouped into i) those

TABLE I
SUMMARY OF THE MAIN FEATURES OF IMPLEMENTED UAV-BASED GPR SYSTEMS

Application	Frequency band (MHz)	Architecture Radar tech.	SAR processing?	Validation scenario	Other specifications	Reference and year
Landmine detection	Between 1500 and 6000	Bistatic (common-offset) SDR radar	No	Loamy soil. 7 m × 5 m 3D volume. Low resolution. Targets at least 20% metal content, buried $\leq$ 20 cm deep.	Flight height $\sim$ 0.5 m	[77], 2017 [78], 2017
Landmine detection primarily	3000 - 5000	DLGPR Pulsed radar	Yes. DAS, [44] PSM, [63]	Sandy soil (sandbox). Vertical cut (2D), 2.5 m long. Metallic and plastic targets, $10 - 15$ cm deep.	Manual flight, $\sim$ 1.5 m high.	[44], 2018 [63], 2019
Generic, detection of buried objects	500 - 2000	DLGPR SFCW radar	Yes	Sandy soil (beach). Vertical cut (2D). Metallic and plastic targets, $5 - 15$ cm deep.	1 Tx antenna 3 Rx antennas Manual flight, $\sim$ 1.5 m high.	[69], 2019
Landmine detection mainly	500 - 3000	Side-looking GPR FMCW radar	Expected	No tests with UAV	Digital Elevation Map (DEM) estimated with a camera	[48], 2019
Landmine detection	1000 - 4000	Side-looking GPR FMCW radar	Yes	Snow sheet 4 cm thick. 6 m × 6 m Metallic targets (aluminum rods and reflectors over ground).	1 Tx antenna 2 Rx antennas (orthogonally arranged) Flight height 3 m	[47], 2019
Landmine detection	1000 - 4000	Side-looking GPR FMCW radar	Circular SAR	Sandy soil. 6.25 m × 5.25 m 3D volume. Metallic and non-metallic targets, between 1 and 15 cm deep.	Flight height from 2.5 m to 5 m, radius of 7.75 m	[49], 2020
Landmine detection	550 - 2700	DLGPR SFCW radar	No	Loamy soil. Vertical cut (2D). Metallic AP landmine, 20 cm deep. Plastic AT landmine, shallow.	Flight height $\leq$ 0.5 m	[79], 2020
Retrieval of snowpack properties	950 - 6000	DLGPR Pseudo-random radar 1 Tx, 2 Rx	No	Snowfields, icesheets. $\approx$ 300 m straight-line scan. Snow depth up to 1.7 m.	Spiral antenna (Tx) 2 Vivaldi antennas (Rx) (orthogonally arranged)	[70], 2020
Retrieval of snowpack properties	700 - 4500	DLGPR Pseudo-random radar 1 Tx, 2 Rx	No	Snowfields, icesheets. 100 m × 100 m scans. 10 m across-track spacing. Snow depth up to 1.53 m.	Dual-Vivaldi	[71], 2020
Archaeological surveys	3100 - 4800	DLGPR Pulse radar	Microwave tomography	Dry soil, archaeological site. 3D imaging.$\sim$ 17 m × 15 m	Flight height from 7.6 m to 10.5 m	[67], 2021
Soil moisture measurement	500 - 700	DLGPR SFCW (VNA)	No	Bare agricultural fields ($\leq$1.40 ha) 1 m along-track meas. sampling. 4 m across-track spacing. From 10 to 20 cm depth.	Flight height from 1 m to 5 m	[74], 2021
Several (infrastructure inspection, archaeological surveys, geological surveys).	200 - 900 and 600 - 1300	DLGPR Pulsed radar [80]	No	Wet sandy soil. Vertical cut (2D). 15 cm and 30 cm diameter buried targets.	Commercial system, independent GPR payload	[81], 2021
Detection of snow avalanche victims	1000 - 4000	Side-looking GPR FMCW radar	Circular SAR	Fresh snow, snowpile $\sim$ 7.5 m × 7.5 m Water-filled canisters and mannequin torso buried up to 40 cm deep.	Flight height from 2 m to 4 m in 0.4 m steps, radius of 7.5 m	[50], 2021
Snow water equivalent content	700 - 4500	DLGPR Pseudo-random radar (1 Tx, 2 Rx)	F - k to estimate velocities	Snowfield. Vertical cut (2D), 250 m long. Snow depth up to 5.5 m.		[64], 2021
Landmine detection primarily	1000 - 4000 for GPR, 6000 - 9000 for InSAR	Side-looking GPR FMCW radar	Circular SAR	Loamy soil. 7.5 m × 6 m 3D volume. Metallic can lids, 5 cm diameter, 5 cm depth.	Flight height 4 m, radius of 7.5 m	[20], 2021
Landmine and IED detection primarily	600 - 6000 (600 -3000 for processing)	DLGPR Pseudo-random radar (1 Tx, 2 Rx)	Yes	Wet loamy soil. 2 m × 10 m [51] Wet loamy soil. 1.5 m × 6 m [58] Dry loamy soil. 4.5 m × 12 m [58] 3D volumes, metallic and plastic targets, up to 25 cm deep.	Flight height 1.2 m - 2.3 m	[51], 2020 [58], 2021
Characterization of a quarry excavation area	20 - 280	DLGPR Pulsed radar [82]	No	Quarry, different kind of rocks. Penetration depth up to 40 m	Flight height 6 m	[73], 2021

which are equal to or smaller than 10 cm, ii) targets whose size ranges from 10 cm to 50 cm, and iii) targets equal to or larger than 50 cm. Finally, targets have been also divided into those that are metallic, and low-metal content / non-metallic targets.

A validation scenario where targets are buried in snow is presented in [50]. It was stated that, in that scenario, the snow had low water content, resulting in a relative permittivity, ε_r, between 2 and 4 [50]. Taking into account the high percentage of water that the human body has, the authors buried water-filled torso-shaped targets to simulate avalanche victims. Thus, for this scenario, a distinction between targets with high water content and low water content will be done.

Detection results of some of the prototypes listed in Table I are summarized in Table II. In order to perform a proper comparison and analysis, only those cases where detailed information about the buried targets and the validation tests is disclosed have been included.

From the detection capabilities summarized in Table II it can be noticed that, as expected, metallic targets provided the best detection results: only small metallic targets (a small disk in [69], and an M14 landmine in [49]), and a metallic can with the lids perpendicular to the soil surface in [58], were missed from the UAV-based GPR prototypes detection.

Concerning the detection of low-metal content or plastic targets, systems enabling SAR processing provided the best detection results. Some of the implemented systems were able to detect small targets (a VS-50 and a PMA-2 anti-personnel landmines in [49], and a PMN-4 anti-personnel landmine in [51]). It is worth mentioning the exhaustive analysis of the detection capabilities presented in [49] and [58], where the validation tests included a wide variety of low-metal content or plastic targets smaller than 50 cm. Furthermore, [58] included tests in dry and wet loamy soils as well.

2D scanning was conducted also with the DLGPR prototype presented in [77], [78], but in this case no SAR processing was applied as no cm-level positioning systems were placed on board the UAV. In spite of this, the prototype was able to detect a PVC pipe-like IED with 30% metal content buried 20 cm deep in a loamy soil.

The rest of the detection results correspond to one along-track flight path, resulting in 2D images (range and along-track cross-range) of the underground. Such configuration required the UAV to fly over the position where the targets were buried (e.g. [44], [69], [79]). In the case of [69], limited across-track cross-range resolution was achieved through the use of a 4-element antenna array. Nevertheless, as shown in Table II, this system was unable to detect non-metallic targets.

Detection results with targets buried in snow were presented in [50]. Targets consisting of empty canisters could not be detected, as opposed to water-filled canisters and mannequin torsos. The reason is that the dielectric contrast between snow ($\varepsilon_r \sim$ 2-4) and water ($\varepsilon_r \sim 80$) is much higher than the dielectric contrast between snow and air ($\varepsilon_r \sim 1$). These promising results are a milestone in the development of UAV-based GPR systems for search and rescue missions of avalanche victims.

Finally, a discussion can be made about which of the UAV-based GPR architectures provides the best detection results. However, this depends on several factors, starting from the targeted application. In this regard, even when focusing on the same application (e.g. landmine and IED detection), the comparison of the detection results achieved with different UAV-based GPR systems is not straightforward. For instance, from the analysis of the detection results shown in Table II, it could be concluded that there are no significant differences between the detection capabilities of the DLGPR architecture presented in [58] and the side-looking CSAR system of [49]. However, the scenarios chosen for the validation tests are different, making it difficult to establish a fair comparison. The fact is that an accurate comparison of the performance of different UAV-based GPR prototypes would require validation tests to be conducted in the same scenario.

IV. Example of UAV-based GPR subsurface imaging

In this Section an application example of the use of a UAV-based GPR system to detect buried targets is presented. The prototype is the one described in [51], [58], consisting of a DLGPR architecture whose working frequency band ranges from 600 MHz to 6000 MHz. From a practical point-of-view, the frequency band selected to process the acquired measurements goes up to 3000 MHz, as higher frequencies are significantly attenuated due to soil propagation losses.

Two scenarios have been considered, each with different characteristics: the first one (Fig. 9 (a)) is within the UAV airfield of the University of Oviedo, located in Gijón, (Spain), being the relative permittivity of the soil ε_r ranging from 6 to 7. The second one (Fig. 9 (b)) is a $4.5\,\text{m} \times 12\,\text{m}$ area within the Spanish Ministry of Defense military training and shooting range "El Palancar" in Madrid (Spain). In this scenario the relative permittivity was found to be $\varepsilon_r \sim 4$.

In all the cases, the UAV performed a zig-zag flight above the scanned area, with an across-track spacing of 5 cm. This spacing corresponds to 0.5λ at 3000 MHz, as required to avoid across-track aliasing when applying GPR-SAR processing (in particular, the DAS method is used). Flight height above the ground was 1.5 m for the first scenario (Fig. 9 (a)), and 1.2 m for the second one (Fig. 9 (b)).

Different targets were buried in these scenarios, mostly consisting of simulants of IEDs, and anti-personnel and anti-tank landmines (some of them can be observed in Fig. 10 and Fig. 11). The size, composition, and burial depth of these targets are given in [58], together with the complete description of the validation tests and detection results. For the sake of clarity, GPR-SAR images corresponding to a VS-1.6 anti-tank landmine [84] will be analyzed in this section, as this target was buried in both scenarios at almost the same depth ($4 - 5$ cm).

DAS method is applied to the geo-referred GPR measurements following the processing steps described in Section II-C. The horizontal (XY plane) and vertical (XZ) cuts of the recovered 3D reflectivity are presented in Fig. 12 for the scenario shown in Fig. 9 (a), and in Fig. 13 for the scenario shown in Fig. 9 (b). z_{est} denotes the depth estimated from the relative permittivity of the soil, calculated as $z_{est} = z/\sqrt{\varepsilon_r}$ (z is the depth assuming free-space propagation).

TABLE II
SUMMARY OF DETECTION CAPABILITIES OF UAV-BASED GPR SYSTEMS

UAV-based GPR system	Metallic targets buried in sandy soils			Non-metallic targets buried in sandy soils		
	Size ≤ 10 cm	Size $10-50$ cm	Size ≥ 50 cm	Size ≤ 10 cm	Size $10-50$ cm	Size ≥ 50 cm
[44], 2018 [63], 2019 DLGPR, SAR 3000 − 5000 MHz		Disk, 12 cm Bar, 12 cm		Box, 9 cm	Disk, 10 cm	
[69], 2019 DLGPR, SAR 500 − 2000 MHz		Large disk, 5 cm, 15 cm (Small disk, 5 cm)	Leaf rake, 0 cm		(Jug, 5 − 31 cm)	(Wooden beam, 5 cm)
[49], 2020 Side-looking, CSAR 1000 − 4000 MHz IEDs and landmines, see Fig. 4 and Fig. 9 of [49].	(M14, 3 cm) DM18B1, 4.5 cm	Projectile, 7 cm		(C3A2, 7 cm) (VS-MK2, 3.5 cm) PMA-2, 4 cm VS-50, 5 cm	(PMA-1A, 3.5 cm) Pressure plate, 14 cm PMN, 6 cm, 10 cm PT-Mi-Ba-III, 15 cm Two PFM-1S, 1 cm PPM-2, 8 cm	
[58], 2021 (scenario 2) DLGPR, SAR 600 − 6000 MHz	Mortar shells, 8 cm				Plastic bag filled with paper, 5 cm Wooden pressure plate, 4 cm Wooden box, 5 − 25 cm Anti-tank landmine VS1.6, 4 cm	

UAV-based GPR system	Metallic targets buried in loamy soils			Non-metallic targets buried in loamy soils		
	Size ≤ 10 cm	Size $10-50$ cm	Size ≥ 50 cm	Size ≤ 10 cm	Size $10-50$ cm	Size ≥ 50 cm
[77], 2017 [78], 2017 Bistatic, no SAR Central freq. 2000 MHz		Two plates, 15 cm Anti-personnel landmine, 10 cm			(Bottle-like IED, 20% metal, 20 cm) PVC pipe-like IED, 30% metal, 20 cm	
[79], 2020 DLGPR, no SAR 550 - 2700 MHz		Anti-personnel landmine, 20 cm			Anti-tank landmine, 0 cm	
[51], 2020 DLGPR, SAR 600 - 6000 MHz		Disk, 25 cm		PMN-4 landmine, 13 cm		
[20], 2021 Side-looking, CSAR 1000 - 4000 MHz	Can lids, 5 cm					
[58], 2021 (scenario 1) DLGPR, SAR 600 - 6000 MHz	Group of metallic plates, 8 cm, 14 cm	(Can, 18 cm) Disk, 9 cm		Landmine TS50, 1 cm (with small Vivaldis)	Trunk-like IED, 1-26 cm Stacked disks, 2-4 cm 7.5 l empty jug, 1-13 cm Anti-tank landmine VS1.6, 5 cm	

UAV-based GPR system	Targets with high water or metallic content buried in snow			Targets with low water or metallic content buried in snow		
	Size ≤ 10 cm	Size $10-50$ cm	Size ≥ 50 cm	Size ≤ 10 cm	Size $10-50$ cm	Size ≥ 50 cm
[50], 2021 Side-looking, CSAR 1000 - 4000 MHz		Mannequin torso (vertical) 35 cm	Mannequin torso, 15 cm (weak at 45 cm) Canisters, 10 cm, 30 cm, 40 cm		(Several empty canisters, 30 cm)	

The value in cm after the target indicates the burial depth.
"Target X, Y cm, Z, cm" indicates that there are several targets X, buried Y cm and Z cm deep.
"Target X, Y-Z, cm" indicates that the depth of the target X ranges from Y cm (top side or face of the target) to Z cm (bottom side or face of the target).
( ) denotes targets not detected or showing unclear detection according to the contribution where detection results were presented.

The VS-1.6 anti-tank landmine is imaged in both scenarios, with a reflectivity peak level of approximately 10 dB above the clutter or background level. The strongest reflection is found at $z_{est} = 11$ cm, which is in agreement with the approximate depth of the bottom of the landmine.

As explained in Section II-B, the reflection happening on top of the landmine is partially masked by the air-ground reflection, whose intensity also depends on the relative permittivity of the soil (the greater the permittivity, the greater the air-soil dielectric contrast). In the second scenario, the soil has lower permittivity than in the first scenario, so the reflection happening on top of the landmine is not fully masked by the air-soil reflection, as observed in the z_{est} = 3.1 cm horizontal cut of Fig. 13.

From the authors' experience with GPR-SAR systems, it has been observed that GPR-SAR images corresponding to soils with high moisture levels usually exhibit more artifacts, thus making the detection of the targets more challenging. This can be observed in the examples presented in Section III of [58]: results depicted in Section III.A correspond to a wet soil whose

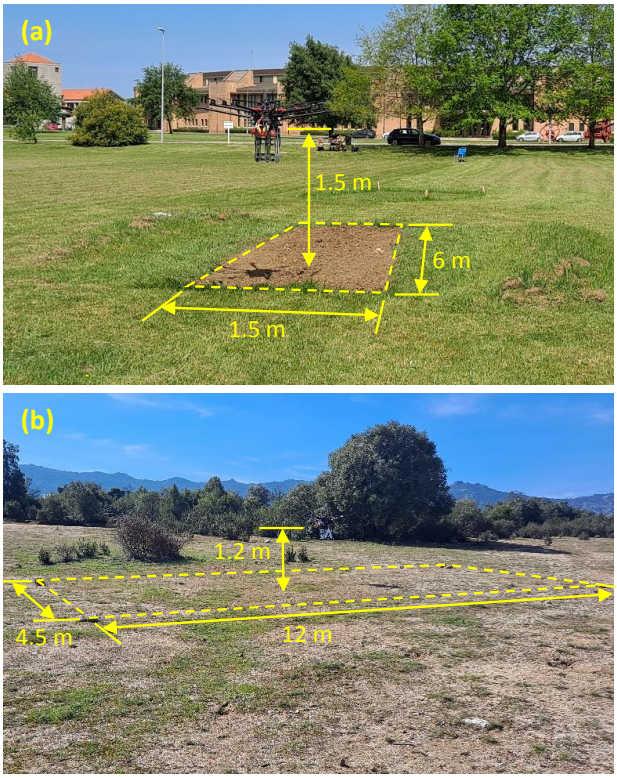

Fig. 9. Picture of a UAV-based GPR prototype scanning the area delimited by the yellow dashed line. (a) Scenario 1 in [58], loamy soil, $\varepsilon_r \sim$ 6-7. (b) Scenario 2 in [58], sandy soil, $\varepsilon_r \sim 4$.

Fig. 10. Picture of some of the targets buried in the scenario shown in Fig. 9 (a), highlighting the VS-1.6 anti-tank landmine (atlm) [84]. (pj) is a 25 l empty plastic jug, and (aplm) is a TS-50 anti-personnel landmine [85].

ε_r is between 6 and 7, whereas the example of Section III.B is for a dry soil with $\varepsilon_r \sim 4$. Quantitatively this means that the reflectivity level of a target with respect to the clutter of the GPR-SAR image is smaller for wet soils (see for example Table 4 of [58]).

V. Challenges and Future Trends

This section discusses some of the challenges faced by UAV-based GPR systems. If the prototypes included in this review are analyzed following a chronological order, it is revealed that technical specifications and detection results have been steadily improved over time. Some of these prototypes can provide 3D images of the subsoil with an approximate resolution of 10 cm (thanks to SAR processing), being able to scan up to 40 m^2 in a single flight.

One of the main challenges faced by UAV-based GPR systems is the extension of the UAV flight time and/or scanning throughput, which can be addressed under the following approaches:

- Use of batteries with improved capacity to battery weight ratio. It must be pointed out that the use of high-capacity batteries does not always result in an extension of the UAV flight time. The reason is that increasing the capacity of the batteries also raises their weight, finding that, sometimes, the additional capacity is not sufficient to compensate for the corresponding increase of the battery weight.

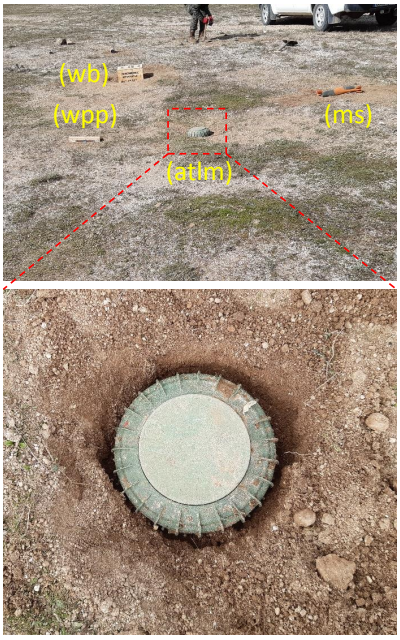

Fig. 11. Picture of some of the targets buried in the scenario shown in Fig. 9 (b), highlighting the VS-1.6 anti-tank landmine (atlm) [84]. (wb) is a wooden box filled with plasterboard, (wpp) is a wooden pressure plate, and (ms) are two metallic mortar shells.

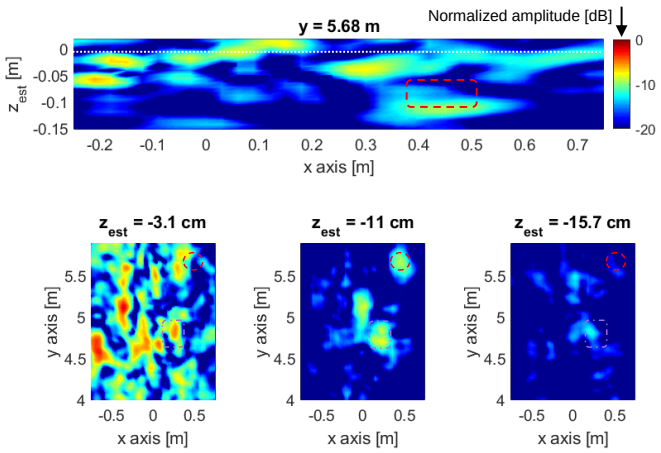

Fig. 12. GPR-SAR imaging results for the scenario shown in Fig. 9 (a). The upper plot corresponds to the vertical cut (XZ plane) centered at the position of the buried VS-1.6 anti-tank landmine. Lower plots represent horizontal cuts (XY plane) at different depths. The white dotted line in the upper plot outlines the position of the air-soil interface. Red dashed lines indicate the profile of the anti-tank landmine, and purple dash-dotted line, the profile of the 25 l plastic jug.

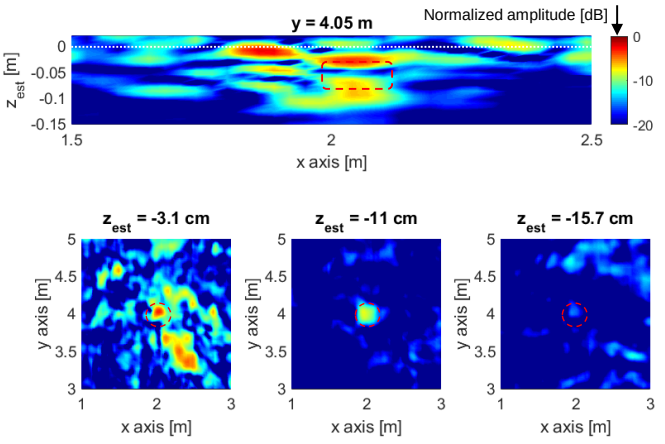

Fig. 13. GPR-SAR imaging results for the scenario shown in Fig. 9 (b). The upper plot corresponds to the vertical cut (XZ plane) centered at the position of the buried VS-1.6 anti-tank landmine. Lower plots represent horizontal cuts (XY plane) at different depths. The white dotted line in the upper plot outlines the position of the air-soil interface. Red dashed lines indicate the profile of the anti-tank landmine.

- Optimization of the UAV payload. Advances in electronics and microwave components miniaturization have resulted in low-cost, lightweight radar modules. However, one of the major bottlenecks is the size (and thus weight) of the antennas to be placed on board the UAV, which is likely to be the bulkiest component, especially if the UAV-based GPR system is intended to operate at sub-GHz frequencies. Although there are several compact, low-cost commercial antennas very suitable for UAV-based GPR systems (a comparison is presented in [58]), a customized antenna design can fit the specifications of a given UAV-based GPR system better than those commercially available.
- Optimization of the scanning strategy. For a single flight, the scanning scheme presented in [20], [49], [50] for side-looking CSAR seems to provide greater scanning throughput than the zig-zag path adopted for UAV-based DLGPR architectures. Conversely, zig-zag paths can fit areas with arbitrary-shaped perimeters, which would result in flight time savings with respect to CSAR-based architectures.
- Increasing the area scanned with a single sweep. In this case, the strategy is to place an antenna array on board the UAV, thus widening the across-track scanned area ([46]). The first attempts have been presented in [69], where thanks to the use of a 4-element antenna array (1 Tx, 3 Rx), 3D images of the subsoil were achieved with a single sweep over the scanned area. A prototype of an antenna array for UAV-GPR applications has been also presented in [86].

Improvement of the GPR resolution is another research topic for future UAV-based GPR systems. As discussed in this review, accurate positioning and geo-referring is a key issue to achieve high-resolution GPR imaging. Advances in GNSS technology have enabled real-time cm-level accuracy positioning. In particular, GNSS-RTK receivers have experienced a steady reduction of their cost while improving their technical features (e.g. multi-frequency and multi-constellation support). In fact, currently several models of consumer drones already include GNSS-RTK technology for accurate flight. Thus, it can be expected that better (and even cheaper) GNSS-RTK receivers will be available in the future, contributing to improving positioning and geo-referring accuracy and, consequently, GPR imaging resolution.

Most of the systems presented in this review are focused on a particular application (e.g. landmine and IED detection, or snowpack thickness measurement). The reason is that the characteristics of the area to be surveyed and the kind of targets to be detected determine the design of the UAV-based GPR system. For example, shallow landmines are difficult to find using a DLGPR system designed to detect larger anti-tank landmines or IEDs buried deep in the ground [54]. Even a commercial general-purpose UAV-based GPR system, like the one developed in [81], needs to be fitted with the proper GPR module depending on the scenario and desired detection capabilities.

The transition from experimental UAV-based GPR prototypes to a ready-to-use system is still ongoing, although some of the prototypes revised in this contribution have been already tested in realistic scenarios. Among them it is possible to cite the tests conducted in [67] concerning archaeological surveys, in [64], [71] for snowpack thickness and snow-water equivalent measurement, in [58] for IED and landmine detection (see Fig. 14), and in [87] for avalanche victims search. In these cases, UAV-based GPR prototypes have faced non-controlled environments like arbitrary soil roughness and moisture, or variable weather conditions. To provide an idea of the challenges to be faced when moving from a realistic validation scenario to a real application case, one can compare the operational conditions found in [50] (realistic, partially controlled scenario) and in [87] (real scenario). In

Fig. 14. UAV-based GPR prototype [58] conducting a validation test for IED detection in an scenario consisting of a dirt road.

both contributions, the goal was the same: the use of a UAV-based GPR system for avalanche victims' search. In the latter contribution, it was described how the UAV-based GPR prototype had to deal with severe weather conditions (quite windy, limiting the UAV capability for a safety flight) and adverse terrain orography (search mission was conducted in a narrow mountain valley, with steep slopes).

Flight regulations is another issue to be taken into account in the development and operation of UAV-based GPR systems. As indicated in [88], UAV regulation is still very dynamic as of 2021 and can be quite different in terms of restrictions from one country to another.

Finally, there are still some scenarios where manned aircrafts are required, as they allow not only heavier payloads but also enable the scanning of larger areas than UAV-based GPR systems. Examples of a helicopter-mounted GPR can be found in [89], [32], and [90]. In these cases, the working frequency of the GPR is smaller than in the UAV-based GPR systems covered in this review: $10-50$ MHz in the case of [90], $50-150$ MHz in [32] (section "Helicopter-borne GPR imaging") and 165, 450, 860 MHz with $40-80$ MHz BW for the GPR system described in [89]. Nevertheless, some of the future trends and improvements outlined in this section could result in the successful replacement of these manned aircrafts by UAV platforms.

VI. Conclusions

A review of the current state-of-the-art on UAV-based GPR systems has been presented in this contribution, focusing on the technical features of the implemented prototypes and how some of these systems have succeeded to obtain 3D cm-level resolution GPR images.

The growing interest in UAV-based GPR systems is supported by the fact that most of the prototypes presented in Table I date from 2020 onwards (see last column of Table I). This has been favored by i) the appearance of compact radiofrequency hardware, ii) affordable cm-level accuracy positioning modules (e.g. multi-band GNSS-RTK receivers), and iii) improvements in consumer drones and UAV technology (e.g. more flexibility for payload integration).

Some of the prototypes have been validated in realistic scenarios [58], [64], [67], [71] and even in real, hazardous environments [87], with at least one commercial system available in the market [81]. Thus, it can be expected that this technology will be soon mature enough to be introduced in other application areas (e.g. civil infrastructure inspection, detection of buried utilities) that involve even more challenging scenarios and flight regulations.

Acknowledgment

The authors would like to thank the personnel of the Counter Improvised Explosive Devices Center of Excellence (C-IED CoE) [91] and the Ministry of Defense of Spain for their counseling and support in the topic of landmine and IED detection. And, in particular, Br. Javier Pacheco Moreno, Col. José Luis Mingote Abad, and Cap. Santiago García Ramos, for their support and help with the validation tests of the UAV-based GPR prototype developed by the University of Oviedo [51], [58] at the Spanish Ministry of Defense military training and shooting range "El Palancar".

References

[1] M. Otten, M. Cuenca, and M. Garcia-Fernandez, "IED command wire detection with multi-channel drone radar," in *Proceedings of the 2021 13th European Conference on Synthetic Aperture Radar (EuSAR)*, 2021, pp. 1185–1188.

[2] A. M. Cunliffe, R. E. Brazier, and K. Anderson, "Ultra-fine grain landscape-scale quantification of dryland vegetation structure with drone-acquired structure-from-motion photogrammetry," *Remote Sensing of Environment*, vol. 183, pp. 129–143, 2016.

[3] T. Adao, J. Hruska, L. Padua, J. Bessa, E. Peres, R. Morais, and J. J. Sousa, "Hyperspectral Imaging: A Review on UAV-Based Sensors, Data Processing and Applications for Agriculture and Forestry," *Remote Sensing*, vol. 9, no. 11, 2017.

[4] J. Evearerts, "The use of unmanned aerial vehicles (UAVs) for remote sensing and mapping," in *The International Archives of the Photogrammetry, Remote Sensing and Spatial Information Sciences*, vol. XXXVII, 2008, pp. 1187–1192.

[5] T.-Z. Xiang, G.-S. Xia, and L. Zhang, "Mini-unmanned aerial vehicle-based remote sensing: Techniques, applications, and prospects," *IEEE Geoscience and Remote Sensing Magazine*, vol. 7, no. 3, pp. 29–63, 2019.

[6] Y. Ham, K. Han, J. Lin, and M. Golparvar-Fard, "Visual monitoring of civil infrastructure systems via camera-equipped Unmanned Aerial Vehicles (UAVs): a review of related works," *Visualization in Engineering*, vol. 4, no. 1, Dec. 2016.

[7] L. M. Gonzalez-deSantos, J. Martinez-Sanchez, H. Gonzalez-Jorge, M. Ribeiro, J. B. de Sousa, and P. Arias, "Payload for Contact Inspection Tasks with UAV Systems," *Sensors*, vol. 19, no. 17, 2019. [Online]. Available: https://www.mdpi.com/1424-8220/19/17/3752

[8] G. Messina and G. Modica, "Applications of UAV Thermal Imagery in Precision Agriculture: State of the Art and Future Research Outlook," *Remote Sensing*, vol. 12, no. 9, 2020.

[9] M. G. Fernandez, Y. A. Lopez, and F. L.-H. Andres, "On the use of unmanned aerial vehicles for antenna and coverage diagnostics in mobile networks," *IEEE Communications Magazine*, vol. 56, no. 7, pp. 72–78, 2018.

[10] A. Salari and D. Erricolo, "Unmanned aerial vehicles for high-frequency measurements: An accurate, fast, and cost-effective technology," *IEEE Antennas and Propagation Magazine*, pp. 2–12, 2021.

[11] J. Burgues and S. Marco, "Environmental chemical sensing using small drones: A review," *Science of The Total Environment*, vol. 748, p. 141172, 2020.

[12] Y. Zhong, X. Wang, Y. Xu, S. Wang, T. Jia, X. Hu, J. Zhao, L. Wei, and L. Zhang, "Mini-UAV-Borne Hyperspectral Remote Sensing: From Observation and Processing to Applications," *IEEE Geoscience and Remote Sensing Magazine*, vol. 6, no. 4, pp. 46–62, 2018.

[13] C. Hügler, F. Roos, M. Schartel, M. Geiger, and C. Waldschmidt, "Radar taking off," *IEEE Microwave Magazine*, vol. 19, pp. 43–53, 2018.

[14] M. Llort, A. Aguasca, C. Lopez-Martinez, and T. Martinez-Marin, "Initial evaluation of SAR capabilities in UAV multicopter platforms," *IEEE Journal of Selected Topics in Applied Earth Observations and Remote Sensing*, vol. 11, pp. 127–140, 2018.

[15] M.-L. Ding, C.-B. Ding, L. Tang, X.-M. Wang, J.-M. Qu, and R. Wu, "A W-band 3-D integrated mini-SAR system with high imaging resolution on UAV platform," *IEEE Access*, vol. 8, pp. 113 601–113 609, 2020.

[16] G. Esposito, C. Noviello, F. Soldovieri, I. Catapano, G. Fasano, G. Gagliarde, G. Luisi, and F. Saccoccio, "The UAV radar imaging prototype developed in the frame of the VESTA project," in *2020 IEEE Radar Conference (RadarConf20)*, 2020, pp. 1–5.

[17] C. J. Li and H. Ling, "High-resolution downward-looking radar imaging using a small consumer drone," in *2016 IEEE AP-S Symposium on Antennas and Propagation*, 2016, pp. 2037–2038.

[18] A. Bekar, M. Antoniou, and C. J. Baker, "Low-Cost, High-Resolution, Drone-Borne SAR Imaging," *IEEE Transactions on Geoscience and Remote Sensing*, pp. 1–11, 2021.

[19] L. Moreira, F. Castro, J. A. Góes, L. Bins, B. Teruel, J. Fracarolli, V. Castro, M. Alcântara, G. Oré, D. Luebeck, L. P. Oliveira, L. Gabrielli, and H. E. Hernandez-Figueroa, "A Drone-borne Multiband DInSAR: Results and Applications," in *2019 IEEE Radar Conference (RadarConf)*, 2019, pp. 1–6.

[20] R. Burr, M. Schartel, A. Grathwohl, W. Mayer, T. Walter, and C. Waldschmidt, "UAV-borne FMCW InSAR for focusing buried objects," *IEEE Geoscience and Remote Sensing Letters*, pp. 1–5, 2021.

[21] Y. S. Alqudsi, A. S. Alsharafi, and A. Mohamed, "A review of airborne landmine detection technologies: Unmanned aerial vehicle-based approach," in *2021 International Congress of Advanced Technology and Engineering (ICOTEN)*, 2021, pp. 1–5.

[22] C.-C. Chen, J. T. Johnson, M. Sato, and A. G. Yarovoy, "Foreword to the Special Issue on Subsurface Sensing Using Ground-Penetrating Radar (GPR)," *IEEE Transactions on Geoscience and Remote Sensing*, vol. 45, no. 8, pp. 2419–2421, 2007.

[23] J. S. Lee, C. Nguyen, and T. Scullion, "A novel, compact, low-cost, impulse ground-penetrating radar for nondestructive evaluation of pavements," *IEEE Transactions on Instrumentation and Measurement*, vol. 53, pp. 1502–1509, 2004.

[24] I. Trinks, A. Hinterleitner, W. Neubauer, E. Nau, K. Löcker, M. Wallner, M. Gabler, R. Filzwieser, J. Wilding, H. Schiel, V. Jansa, P. Schneidhofer, T. Trausmuth, V. Sandici, D. Ruß, S. Flöry, J. Kainz, M. Kucera, A. Vonkilch, T. Tencer, L. Gustavsen, M. Kristiansen, L.-M. Bye-Johansen, C. Tonning, T. Zitz, K. Paasche, T. Gansum, and S. Seren, "Large-area high-resolution ground-penetrating radar measurements for archaeological prospection," *Archaeological Prospection*, vol. 25, no. 3, pp. 171–195, 2018. [Online]. Available: https://onlinelibrary.wiley.com/doi/abs/10.1002/arp.1599

[25] D. J. Daniels, "A review of GPR for landmine detection," *Sensing and Imaging: an International Journal*, vol. 7, pp. 90–123, 2006.

[26] (2021, 5) Minekafon project. [Online]. Available: http://minekafon.org/

[27] A. Selvarajan and H. Yogaraju, "Design and development of a quadcopter for landmine detection," in *2020 IEEE Student Conference on Research and Development (SCOReD)*, 2020, pp. 80–85.

[28] L.-S. Yoo, J.-H. Lee, S.-H. Ko, S.-K. Jung, S.-H. Lee, and Y.-K. Lee, "A drone fitted with a magnetometer detects landmines," *IEEE Geoscience and Remote Sensing Letters*, vol. 17, no. 12, pp. 2035–2039, 2020.

[29] C. J. Leuschen and R. G. Plumb, "A matched-filter-based reverse-time migration algorithm for ground-penetrating radar data," *IEEE Transactions on Geoscience and Remote Sensing*, vol. 39, pp. 929–936, 2001.

[30] H. M. Jol, *Ground Penetrating Radar: Theory and Applications*. Amsterdam: Elsevier, 2009.

[31] N. Diamanti and A. P. Annan, "Air-launched and ground-coupled GPR data," in *2017 11th European Conference on Antennas and Propagation (EUCAP)*, 2017, pp. 1694–1698.

[32] I. Catapano, G. Gennarelli, G. Ludeno, C. Noviello, G. Esposito, and F. Soldovieri, "Contactless ground penetrating radar imaging: State of the art, challenges, and microwave tomography-based data processing," *IEEE Geoscience and Remote Sensing Magazine*, pp. 2–24, 2021.

[33] E. M. Rosen and E. Ayers, "Assessment of down-looking GPR sensors for landmine detection," in *Detection and Remediation Technologies for Mines and Minelike Targets X*, R. S. Harmon, J. T. Broach, and J. H. H. Jr., Eds., vol. 5794, International Society for Optics and Photonics. SPIE, 2005, pp. 423 – 434. [Online]. Available: https://doi.org/10.1117/12.603831

[34] A. Moreira, P. Prats-Iraola, M. Younis, G. Krieger, I. Hajnsek, and K. P. Papathanassiou, "A tutorial on synthetic aperture radar," *IEEE Geoscience and Remote Sensing Magazine*, vol. 1, no. 1, pp. 6–43, 2013.

[35] W. Stempfhuber and M. Buchholz, "A precise, low cost RTK GNSS system for UAV applications," in *Int. Arch. Photogramm. Remote Sens. Spatial Inf. Sci.*, vol. XXXVIII, no. 1/C22, 2011, p. 289–293.

[36] (2021, 5) DRTK GNSS from DJI. [Online]. Available: https://www.dji.com/d-rtk/info

[37] (2021, 9) Precise Point Positioning (PPP). [Online]. Available: https://novatel.com/an-introduction-to-gnss/chapter-5-resolving-errors/precise-point-positioning-ppp

[38] M. Schartel, R. Burr, P. Schoeder, G. Rossi, P. Hügler, W. Mayer, and C. Waldschmidt, "Radar-based altitude over ground estimation of UAVs," in *Proc. of the 3rd International Workshop on Advanced Ground Penetrating Radar (IWAGPR)*, 2018, pp. 103–106.

[39] C. N. Koyama, H. Liu, K. Takahashi, M. Shimada, M. Watanabe, T. Khuut, and M. Sato, "In-situ measurement of soil permittivity at various depths for the calibration and validation of low-frequency sar soil moisture models by using gpr," *Remote Sensing*, vol. 9, no. 6, 2017. [Online]. Available: https://www.mdpi.com/2072-4292/9/6/580

[40] S. Paul, R. Chugh, and M. J. Akhtar, "Microwave Synthetic Aperture Radar Imaging Using SFCW System for Buried Object Detection and Security Applications," in *2019 IEEE MTT-S International Microwave and RF Conference (IMARC)*, 2019, pp. 1–4.

[41] D. Wang, S. Yoo, and S. H. Cho, "Experimental Comparison of IR-UWB Radar and FMCW Radar for Vital Signs," *Sensors*, vol. 20, no. 22, 2020. [Online]. Available: https://www.mdpi.com/1424-8220/20/22/6695

[42] L. Tantiparimongkol and P. Phasukkit, "IR-UWB Pulse Generation Using FPGA Scheme for through Obstacle Human Detection," *Sensors*, vol. 20, no. 13, 2020. [Online]. Available: https://www.mdpi.com/1424-8220/20/13/3750

[43] (2021, 7) Meet the open-source software powering NASA's ingenuity mars helicopter. [Online]. Available: https://www.jpl.nasa.gov/news/meet-the-open-source-software-powering-nasas-ingenuity-mars-helicopter

[44] M. Garcia-Fernandez, Y. Alvarez-Lopez, A. Arboleya-Arboleya, B. Gonzalez-Valdes, Y. Rodriguez-Vaqueiro, F. Las-Heras, and A. Pino-Garcia, "Synthetic aperture radar imaging system for landmine detection using a ground penetrating radar on board a unmanned aerial vehicle," *IEEE Access*, vol. 6, pp. 45 100–45 112, 2018.

[45] D. Comite, F. Ahmad, T. Dogaru, and M. G. Amin, "Adaptive Detection of Low-Signature Targets in Forward-Looking GPR Imagery," *IEEE Geoscience and Remote Sensing Letters*, vol. 15, pp. 1520–1524, 2018.

[46] D. Comite, F. Ahmad, M. G. Amin, and T. Dogaru, "Forward-Looking Ground-Penetrating Radar: Subsurface Target Imaging and Detection: A Review," *IEEE Geoscience and Remote Sensing Magazine*, vol. Early Access, pp. 0–0, 2021.

[47] R. Burr, M. Schartel, W. Mayer, T. Walter, and C. Waldschmidt, "UAV-Based Polarimetric Synthetic Aperture Radar for Mine Detection," in *IGARSS 2019 - 2019 IEEE International Geoscience and Remote Sensing Symposium*, 2019, pp. 9208–9211.

[48] E. Schreiber, A. Heinzel, M. Peichl, M. Engel, and W. Wiesbeck, "Advanced buried object detection by multichannel, UAV/drone carried synthetic aperture radar," in *Proceedings of the 2019 13th European Conference on Antennas and Propagation (EuCAP)*, 2019, pp. 1–5.

[49] M. Schartel, R. Burry, R. Bahnemannz, W. Mayer, and C. Waldschmidt, "An Experimental Study on Airborne Landmine Detection Using a Circular Synthetic Aperture Radar," 2020. [Online]. Available: https://arxiv.org/abs/2005.02600

[50] A. Grathwohl, P. Hinz, R. Burr, M. Steiner, and C. Waldschmidt, "Experimental study on the detection of avalanche victims using an airborne ground penetrating synthetic aperture radar," in *2021 IEEE Radar Conference (RadarConf21)*, 2021, pp. 1–6.

[51] M. Garcia-Fernandez, Y. Alvarez-Lopez, and F. Las-Heras, "Airborne multi-channel ground penetrating radar for improvised explosive devices and landmine detection," *IEEE Access*, vol. 8, pp. 165 927–165 943, 2020.

[52] P. Annan. (2019, 1) Ground penetrating radar (GPR) and drones – double jeopardy! [Online]. Available: https://www.sensoft.ca/gpr/gpr-and-drones-double-jeopardy/

[53] M. Garcia-Fernandez, A. Morgenthaler, Y. Alvarez-Lopez, F. Las Heras, and C. Rappaport, "Bistatic Landmine and IED Detection Combining Vehicle and Drone Mounted GPR Sensors," *Remote Sensing*, vol. 11, no. 19, 2019.

[54] M. García-Fernández, G. Álvarez Narciandi, Y. Álvarez López, and F. Las-Heras Andrés, "Analysis and validation of a hybrid forward-looking down-looking ground penetrating radar architecture," *Remote Sensing*, vol. 13, no. 6, 2021.

[55] M. Gonzalez-Diaz, M. Garcia-Fernandez, Y. Alvarez-Lopez, and F. Las-Heras, "Improvement of GPR SAR-based techniques for accurate detection and imaging of buried objects," *IEEE Transactions on Instrumentation and measurement*, vol. 6, pp. 3126–3138, 2020.

[56] M. Garcia-Fernandez, Y. Alvarez-Lopez, and F. Las-Heras, "Autonomous airborne 3D SAR imaging system for subsurface sensing: UWB-GPR on board a UAV for landmine and IED detection," *Remote Sensing*, vol. 11, p. 2357, 2019.

[57] M. Garcia-Fernandez, Y. Alvarez-Lopez, Y. Rodriguez-Vaqueiro, B. Gonzalez-Valdes, A. Arboleya-Arboleya, F. Las-Heras, and A. Pino-Garcia, "SVD-based clutter removal technique for GPR," in *2017 IEEE AP-S Symposium on Antennas and Propagation*, 2017, pp. 2369–2370.

[58] M. Garcia-Fernandez, G. Alvarez-Narciandi, A. Arboleya-Arboleya, C. Vazquez-Antuña, F. Las-Heras, and Y. Alvarez-Lopez, "Development of an airborne-based GPR system for landmine and IED detection: antenna analysis and intercomparison," *IEEE Access*, 2021.

[59] S. Khudoyarov, N. Kim, and J.-J. Lee, "Three-dimensional convolutional neural network–based underground object classification using three-dimensional ground penetrating radar data," *Structural Health Monitoring*, vol. 19, pp. 1884–1893, 2020.

[60] E. M. Johansson and J. E. Mast, "Three-dimensional ground-penetrating radar imaging using synthetic aperture time-domain focusing," in *Advanced Microwave and Millimeter-Wave Detectors*, S. S. Udpa and H. C. Han, Eds., vol. 2275, International Society for Optics and Photonics. SPIE, 1994, pp. 205 – 214. [Online]. Available: https://doi.org/10.1117/12.186717

[61] D. H. N. Marpaung and Y. Lu, "A comparative study of migration algorithms for UWB GPR images in SISO-SAR and MIMO-array configurations," in *15th IEEE International Radar Symposium (IRS)*, 2014, pp. 1–4.

[62] C. Ozdemir, S. Demirci, E. Yigit, and B. Yilmaz, "A Review of Migration Methods in B-Scan Ground Penetrating Radar Imaging," *Mathematical Problems in Engineering*, vol. 2014, pp. 1–16, 2014.

[63] M. Garcia-Fernandez, Y. Alvarez-Lopez, B. Gonzalez-Valdes, Y. Rodriguez-Vaqueiro, A. Arboleya-Arboleya, and F. L. Heras, "Recent advances in high-resolution ground penetrating radar on board an unmanned aerial vehicle," in *2019 13th European Conference on Antennas and Propagation (EuCAP)*, 2019, pp. 1–5.

[64] R. O. R. Jenssen and S. K. Jacobsen, "Measurement of Snow Water Equivalent Using Drone-Mounted Ultra-Wide-Band Radar," *Remote Sensing*, vol. 13, no. 13, 2021. [Online]. Available: https://www.mdpi.com/2072-4292/13/13/2610

[65] M. Fallahpour, J. T. Case, M. T. Ghasr, and R. Zoughi, "Piecewise and wiener filter-based SAR techniques for monostatic microwave imaging of layered structures," *IEEE Transactions on Antennas and Propagation*, vol. 62, pp. 282–294, 2014.

[66] G. Ludeno, G. Gennarelli, S. Lambot, F. Soldovieri, and I. Catapano, "A comparison of linear inverse scattering models for contactless gpr imaging," *IEEE Transactions on Geoscience and Remote Sensing*, vol. 58, no. 10, pp. 7305–7316, 2020.

[67] C. Noviello, G. Esposito, I. Catapano, and F. Soldovieri, "Multilines Imaging Approach for Mini-UAV Radar Imaging System," *IEEE Geoscience and Remote Sensing Letters*, vol. 1, pp. 1–5, 2021.

[68] Y. Alvarez, M. Garcia, A. Arboleya, B. Gonzalez, Y. R. Vaqueiro, F. Las-Heras, and A. G. Pino, "SAR-based technique for soil permittivity estimation," *International Journal of Remote Sensing*, vol. 38, pp. 5168–5186, 2017.

[69] C. Roussi, I. Xique, J. Burns, and B. Hart, "Buried object imaging using a small UAS-based GPR," in *Proceedings of the SPIE 11012, Detection and Sensing of Mines, Explosive Objects, and Obscured Targets XXIV*, vol. 11012, 2019, pp. 1–9.

[70] R. O. R. Jenssen, M. Eckerstorfer, and S. Jacobsen, "Drone-mounted ultrawideband radar for retrieval of snowpack properties," *IEEE Transactions on Instrumentation and Measurement*, vol. 69, no. 1, pp. 221–230, 2020.

[71] R. O. R. Jenssen and S. Jacobsen, "Drone-mounted UWB snow radar: technical improvements and field results," *Journal of Electromagnetic Waves and Applications*, vol. 34, no. 14, pp. 1930–1954, 2020.

[72] K. V. Mazalevskiy, "The remote sensing of snow water equivalent using broadband electromagnetic pulses from an UAV board," *Journal of Radio Electronics*, vol. 8, 2021. [Online]. Available: http://jre.cplire.ru/jre/aug21/1/abstract_e.html

[73] A. Saponaro, G. Dipierro, E. Cannella, A. Panarese, A. M. Galiano, and A. Massaro, "A UAV-GPR Fusion Approach for the Characterization of a Quarry Excavation Area in Falconara Albanese, Southern Italy," *Drones*, vol. 5, no. 2, 2021. [Online]. Available: https://www.mdpi.com/2504-446X/5/2/40

[74] K. Wu, G. A. Rodriguez, M. Zajc, E. Jacquemin, M. Clément, A. De Coster, and S. Lambot, "A new drone-borne GPR for soil moisture mapping," *Remote Sensing of Environment*, vol. 235, p. 111456, 2019. [Online]. Available: https://www.sciencedirect.com/science/article/pii/S0034425719304754

[75] (2021, 5) Spreading windws s1000+ from DJI. [Online]. Available: https://www.dji.com/spreading-wings-s1000-plus

[76] (2021, 9) Matrice 600 pro from DJI. [Online]. Available: https://www.dji.com/matrice600-pro

[77] J. Colorado, M. Perez, I. Mondragon, D. Mendez, C. Parra, C. Devia, J. Martinez-Moritz, and L. Neira, "An integrated aerial system for landmine detection: SDR-based ground penetrating radar onboard an autonomous drone," *Advanced Robotics*, vol. 31, pp. 791–808, 2017.

[78] M. R. P. Cerquera, J. D. C. Montaño, and I. Mondragon, "UAV for Landmine Detection Using SDR-Based GPR Technology," in *Robots Operating in Hazardous Environments*, H. Canbolat, Ed. Rijeka: IntechOpen, 2017, ch. 2. [Online]. Available: https://doi.org/10.5772/intechopen.69738

[79] D. Sipos and D. Gleich, "A lightweigth and low-power UAV-borne ground penetrating radar design for landmine detection," *Sensors*, vol. 20, p. 2234, 2020.

[80] (2021, 9) Zond-12e Advanced GPR from Radar Systems. [Online]. Available: http://www.radsys.lv/en/products-soft/products/prod/4

[81] (2017, 10) Drone equipped with ground penetrating radar (GPR). [Online]. Available: https://integrated.ugcs.com/gpr

[82] (2021, 9) COBRA plug-in SE-150 from Radarteam Sweden AB. [Online]. Available: http://www.radarteam.se/COBRA_PLUGIN_GPR_web.pdf

[83] S. Prager and M. Moghaddam, "Application of Ultra-Wideband Synthesis in Software Defined Radar for UAV-based Landmine Detection," in *IGARSS 2019 - 2019 IEEE International Geoscience and Remote Sensing Symposium*, 2019, pp. 10 115–10 118.

[84] (2021, 5) VS-1.6 anti-tank landmine. [Online]. Available: https://en.wikipedia.org/wiki/VS-1.6_mine

[85] (2021, 5) TS-50 anti-personnel landmine. [Online]. Available: https://en.wikipedia.org/wiki/TS-50_mine

[86] Y. Rodriguez-Vaqueiro, J. Vázquez-Cabo, B. Gonzalez-Valdes, A. Pino, Y. Álvarez, M. Garcia-Fernandez, F. Las-Heras, and A. Arboleya, "Array of Antennas for a GPR system onboard a UAV," in *2019 IEEE International Symposium on Antennas and Propagation and USNC-URSI Radio Science Meeting*, 2019, pp. 821–822.

[87] (2021, 5) Using a Drone-based Ground Penetrating Radar for Avalanche Victim Search: A Case Study from Northern Spain from UGCS. [Online]. Available: https://http://www.radsys.lv/userfiles/files/avalanche-victim-search-report.pdf

[88] J. Francke and A. Dobrovolskiy, *Challenges and opportunities with drone-mounted GPR*, 2021, pp. 3043–3047. [Online]. Available: https://library.seg.org/doi/abs/10.1190/segam2021-3582927.1

[89] G. Gennarelli, I. Catapano, G. Ludeno, C. Noviello, C. Papa, G. Pica, F. Soldovieri, and G. Alberti, "A low frequency airborne GPR system for wide area geophysical surveys: The case study of morocco desert," *Remote Sensing of Environment*, vol. 233, p. 111409, 2019. [Online]. Available: https://www.sciencedirect.com/science/article/pii/S0034425719304286

[90] D. Edemsky, A. Popov, I. Prokopovich, and V. Garbatsevich, "Airborne ground penetrating radar, field test," *Remote Sensing*, vol. 13, no. 4, 2021. [Online]. Available: https://www.mdpi.com/2072-4292/13/4/667

[91] (2021, 5) Counter improvised explosive devices center of excellence (C-IED CoE). [Online]. Available: https://www.ciedcoe.org/